

# Fast functional magnetic resonance imaging—a new approach towards neuroimaging

CUN-HUI ZHANG\*, MARTIN A. LINDQUIST, ZANG-HEE CHO,  
GARY GLOVER AND LAWRENCE SHEPP\*

---

Functional MRI, a powerful method of neuroimaging, is expected to have profound and far-reaching consequences in the understanding of human brain function, a problem of central scientific interest at the present time. However, for higher cognition studies, the *time-resolution* of present techniques has to be greatly improved. In this paper, we describe a fast functional MRI approach which we have developed, including an echo-volumar imaging sampling scheme, image reconstruction based on prolate-spheroidal kernels, optimality properties of these sampling and image reconstruction methods, and statistical analysis of fast functional MRI data. Results from real experiments are presented to demonstrate the feasibility of our methods.

KEYWORDS AND PHRASES: Functional MRI, Rapid imaging, Echo-volumar imaging, Single-shot imaging, Hemodynamic response, Positive rise, Negative dip, Temporal resolution, Prolate-spheroidal wave function, Time series, False discovery rate, Bootstrap.

---

## 1. INTRODUCTION

Functional magnetic resonance imaging (fMRI) studies the location and time of brain activity produced by mental tasks. In an fMRI experiment, the brain is repeatedly scanned to measure changes in blood flow and oxygenation, which are known to be correlated to neural activities.

A standard technique in fMRI research uses Ogawa's [21, 19, 20] blood oxygen level dependent (BOLD) method to detect changes in magnetic susceptibility due to the resupply of oxygenated blood to capillaries near areas of neural activity. Hemoglobin exists in two states, oxygenated and deoxygenated, respectively having negative and positive magnetic susceptibility. When neural activity uses oxygen locally stored in hemoglobin, the cerebral blood flow subsequently overcompensates this consumption, causing a relatively high concentration of oxygenated hemoglobin. This results in a signal called the *positive rise* in the hemodynamic response.

A serious problem with studying the rise, especially for research in human higher cognition, is that this signal is far removed from the underlying neuronal activity. The positive

rise has a delay of about 2 seconds and peaks at 5 seconds or more after neural activity, while most higher cognition processes take place within a fraction of a second. Since the amount of delay and time-to-peak are neither homogeneous nor synchronized, the positive rise carries very little information about the timing or ordering of neural activities in different parts of the brain. The aim of fast fMRI (ffMRI) is to overcome this difficulty by sharply improving the time-resolution of the technology, and by concentrating the statistical analysis on signals that appear within the first second of activation.

Our approach [24, 30, 11–14] is to measure the so-called fast *negative dip* phenomenon of BOLD fMRI [2, 4, 18, 15, 29, 3, 10, 26]. Local oxygen consumption creates a relatively high concentration of deoxygenated hemoglobin before the blood resupply arrives and consequently must cause an initial negative dip within a second or so in the hemodynamic response. The question is whether this signal can be reliably measured to study brain function. The standard fMRI methodologies, which scan the brain at the rate of about every other second, are too slow to capture the negative dip. We have developed an echo-volumar imaging (EVI) sampling scheme for ffMRI, which maps the brain at the rate of every 100 ms, along with the necessary tools for image reconstruction and statistical analysis. In our experiments, the negative dip is statistically significant in multiple primary brain regions which match the activation paradigms. Our goal is to observe similar fast negative dips in secondary brain regions where higher level brain processing takes place in image understanding and other higher cognition tasks. If secondary negative dips can be detected in the right time scale then the time sequence of the subtasks of a given task would allow determination of the parts of the brain involved and by using the commonality between subtasks of different tasks, and logic, a more complete mapping of higher level brain function may be obtained.

We have made good progress but we still need to incorporate new advances in MRI technology and fully develop our methodologies. We have conducted experiments with 3 T (tesla) and 1.5 T MRI scanners, but the new, more powerful 7 T scanners have produced images of far better resolution. Figure 1, considered by leading experts as an MRI image of uniformly the finest resolution, clearly demonstrates the advantages of the 7 T technology. However, 7 T MRI has to

---

\*Research partially supported by NSF Grant DMS 0504387.

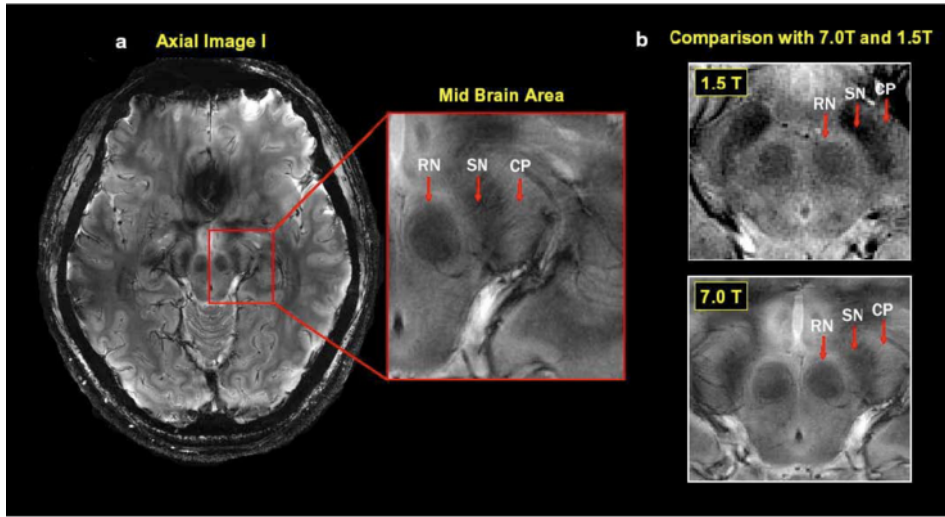


Figure 1. (a) An Axial Image of Human Brain in-vivo Obtained at the Neuroscience Research Institute, Gachon University of Medicine and Science, Incheon, Korea, by 7.0 T MRI with a Brain-Optimized SENSE (SENSitivity Encoded) RF Coil. The Area Shown Is the Midbrain Showing the Red Nucleus (RN), the Cerebral Peduncle (CP), and the Substantia Nigra (SN), Among Other Regions. In the Middle, We Show the Expanded View of the Central Part of the Image Which Clearly Delineates the Above Three Nuclei. (b) Comparison of the Images of the Midbrain Area Obtained by 7.0 T and 1.5 T where Substantia Nigra, Cerebral Peduncle, and Red Nucleus Are Located. Note the Improved Image Quality of 7.0 T Compared with 1.5 T.

deal with extremely delicate issues of field distortion, susceptibility, radio frequency inhomogeneity and more. In particular, the feasibility of fMRI at 7 T is questionable due to susceptibility artifacts. To settle this feasibility question, we must conduct 7 T experiments with a carefully designed multiple receiver coil system, and we must develop new statistical methodologies to treat such multi-coil fMRI data.

The rest of the paper describes the methodologies we have developed so far, reports the results of our most recent experiments and discusses some directions of further research in fMRI.

## 2. FAST FMRI DATA ACQUISITION

In this section, we describe MR signals, fMRI image sequences and the EVI sampling scheme. For simplicity and with minimum loss of generality, much of the discussion uses the specifications of our 2006 experiments with the 3 T GE scanner at the Stanford MRI Lab.

### 2.1 Free induction decay signals

A basic MR signal is provided in the free induction decay after the excitation of the nuclear spin field of an object by a radio frequency pulse. The signal, encoded almost continuously during a readout period as the electromagnetic induction with a receiver coil, can be viewed as the integration of the nuclear spin. A system of gradient coils is used to sequentially control the spatial inhomogeneity of the magnetic field, so that each measurement of the signal can be approximately expressed as the Fourier transformation of the spin

density at a single point in the frequency domain called  $k$ -space. Mathematically, the measurement of the MR signal in the  $j$ -th time unit of a readout period can be written as

$$(2.1) \quad S(\mathbf{k}(t_j)), \quad \text{where } S(\mathbf{k}) \approx \int_{\Omega} f(\mathbf{v}; t_j) \exp(i\mathbf{v}'\mathbf{k}) d\mathbf{v},$$

$t_j = j\Delta_t$  is the time of the measurement,  $\Omega$  is the space of the spin system,  $f(\mathbf{v}; t_j)$ , defined for  $\mathbf{v} \in \Omega$ , is the spin density at time  $t_j$ , and  $\mathbf{k}(t_j)$  is the point in  $k$ -space at which the Fourier transformation is measured. In our 2006 experiments with the 3 T GE scanner,  $\Delta_t = 4 \mu\text{s}$  (microsecond), the total length of a single readout period is approximately 47 ms (millisecond), and the total time cost for a single shot, including an excitation followed by encoding in a readout period, is  $T_{shot} = 100$  ms.

### 2.2 Functional MRI image sequence and time resolution

In an fMRI experiment, a subject repeatedly performs certain mental tasks according to an activation paradigm while  $k$ -space measurements are taken in a succession of alternating excitation and readout periods in each replication of the mental tasks. The time variable  $t_j = j\Delta_t$  in (2.1) is reset to zero at the beginning of each readout period. Thus, in the  $m$ -th readout period, the actual time for the encoding of (2.1) is  $(m-1)T_{shot} + t_j$  and the function  $f(\mathbf{x}; t_j)$  in (2.1) is actually the spin density at the time  $(m-1)T_{shot} + t_j$ . If  $m$  excitation shots are needed to encode the data for one image, the underlying assumption is that the spin density

is essentially unchanged in a time period of length  $mT_{shot}$ . Most signals of temporal resolution faster than  $mT_{shot}$  will be lost with such  $m$ -shot schemes.

If all brain regions of interest lie very close to a known single plane, radio frequency pulses can be tailored to excite only a thin slice of the brain containing the known plane, so that the field  $\Omega$  in (2.1) is two-dimensional. In this case, a single readout period is sufficient to sample the two-dimensional  $k$ -space at the  $64 \times 64$  spatial resolution. Since our goal is to study higher level brain functions in possibly unknown regions, the focus of this paper is 3D fMRI. In this case, quite a few shots are needed to sample the entire 3D  $k$ -space.

A standard imaging sequence divides the 3D field  $\Omega$  into  $m$   $64 \times 64$  slices and uses a single shot to acquire full  $k$ -space data for each slice. For  $m = 20$  and  $T_{shot} = 100$  ms, the resulting time resolution  $mT_{shot} = 2$  s is too slow for studying human higher cognition. Since the data acquisition for the 2D image of each slice is completed within a single shot, some signals of higher temporal resolution than 2 s may still be captured by imaging different slices at the beginning of different replication cycles of the experimental paradigm. However, since the number of replications allocated to each time unit of the experimental paradigm is proportional to the length of the time unit, this trick requires a large total number of replication cycles to acquire sufficient information for signals much faster than 2 s. Thus, it can be implemented only to a limited extent due to machine availability constraints and subject fatigue.

In the 2006 experiments, our methodologies provide an estimate of a smooth version of the entire 3D-spin density in the brain based on  $k$ -space signals following a single excitation pulse. Thus, the time resolution of our imaging sequence is identical to  $T_{shot} = 100$  ms. Of course, some spatial resolution is sacrificed for the 20 fold gain in time resolution.

### 2.3 The EVI trajectory

Since our goal is to use the fast negative dip to study brain function, we set the time resolution of our fMRI imaging sequence at  $T_{shot} = 100$  ms with the 3 T GE scanner. The remaining design question is to choose a sequence of  $k$ -space points  $\mathbf{k}(t_j)$  in (2.1) within a single shot to (nearly) optimize the spatial resolution of the image, subject to machine constraints and convenience in image reconstruction and statistical analysis.

Let  $\mathbf{g}(t_j) \in \mathbb{R}^3$  and  $\mathbf{s}(t_j) \in \mathbb{R}^3$  be the discrete gradient and slew rate of the  $k$ -space trajectory:

$$\mathbf{g}(t_j) = \frac{\mathbf{k}(t_j) - \mathbf{k}(t_{j-1})}{\gamma \Delta_t}, \quad \mathbf{s}(t_j) = \frac{\mathbf{g}(t_j) - \mathbf{g}(t_{j-1})}{\Delta_t},$$

where  $\Delta_t = t_j - t_{j-1} = 4 \mu\text{s}$  and  $\gamma$  is the gyromagnetic ratio. In our experiment,  $\gamma = 42.58 \text{ MHz T}^{-1}$  for  $^1\text{H}$ , and the machine constraints are

$$(2.2) \quad \|\mathbf{g}(t_j)\| \leq 4 \text{ G/cm}, \quad \|\mathbf{s}(t_j)\| \leq 15 \text{ G/cm/ms}.$$

The image reconstruction issues are best described in terms of the discrete Fourier transformation. Consider a 3D cube  $\Omega$  of size  $\text{FOV}^3$  centered at  $(0, 0, 0)$ , with the field of view  $\text{FOV} \approx 20$  cm. For  $n \times n \times n$  spatial resolution, we divide  $\Omega$  into a lattice of  $n^3$  voxels and approximate the signal (2.1) by its discrete version as

$$(2.3) \quad S(\mathbf{k}(t_j)) \approx S_d(\mathbf{k}(t_j)), \\ S_d(\mathbf{k}) = \sum_{\mathbf{v} \in \Omega_d} f(\mathbf{v}) \exp(i\mathbf{v}'\mathbf{k}) \{\text{FOV}/n\}^3,$$

where  $\Omega_d$  is the set of the centers of the  $n^3$  voxels and the spin density is treated as identical within the readout period. The Fourier inversion gives

$$(2.4) \quad f(\mathbf{v}) = \sum_{\mathbf{k} \in \Omega_d^*} S_d(\mathbf{k}) \exp(-i\mathbf{v}'\mathbf{k}) / \text{FOV}^3, \quad \forall \mathbf{v} \in \Omega_d,$$

where  $\Omega_d^* = (2\pi n / \text{FOV}^2) \Omega_d$ . Since  $\Omega_d$  is a 3D lattice with span  $\text{FOV}/n$  in each coordinate,  $\Omega_d^*$  is a lattice with span  $\Delta_k = 2\pi / \text{FOV}$ . Since  $(\exp(i\mathbf{v}'\mathbf{k}), \mathbf{v} \in \Omega_d)$  are orthogonal vectors for  $\mathbf{k} \in \Omega_d^*$  and  $\Delta_k$  is independent of the spatial resolution level, for image reconstruction and statistical analysis purposes, it is convenient to require the trajectory  $\mathbf{k}(t)$  to traverse through a cubic or hyper-rectangular lattice  $A_d$  of span  $\Delta_k$  inside  $\Omega_d^*$ .

Here is a brief description of our EVI trajectory [13, 14]. Given the total time  $T$  of a reading period and the shape and span  $\Delta_k$  of the  $k$ -space lattice  $A_d$  to be sampled, the optimization problem is to maximize the size of  $A_d$  covered by a smooth curve  $\{\mathbf{k}(t), 0 \leq t \leq T\}$  satisfying the machine constraints  $\|\mathbf{k}'(t)\| \leq 4\gamma$  and  $\|\mathbf{k}''(t)\| \leq 15\gamma$  in (2.2) and the boundary conditions  $\mathbf{k}(0) = \mathbf{k}'(0) = (0, 0, 0)$ . We consider the class of all such curves composed of line segments parallel to the  $z$ -axis in  $k$ -space and half circles to change the  $x$ - $y$  position among the different line segments. We prove that the optimal solution is to set the diameter of the half circles to  $\Delta_k$ , and to maximize the acceleration (deceleration) toward (from) the middle of each line segment in the  $z$ -direction, provided the condition  $\|\mathbf{k}'(t)\| \leq 4\gamma$  for the gradient. Since we wish to sample the center of  $k$ -space at the beginning of the readout period when the SNR is high, the projection of our EVI trajectory to the  $x$ - $y$  plane is a square spiral beginning from the origin. This EVI trajectory, plotted in Figure 2, visits 11796 points in one readout period of  $11796 \times 4 \mu\text{s} \approx 47$  ms to cover a  $14 \times 14 \times 17 \Delta_k^3$  hyperrectangle in the center of  $k$ -space, with  $\text{FOV} = 2\pi\Delta_k = 24$  cm. Different types of EVI trajectories were considered earlier in [17, 16, 8].

## 3. IMAGE RECONSTRUCTION AND STATISTICAL ANALYSIS

We discuss in this section methodologies for image reconstruction, statistical inference and visualization. We begin with description of a real fMRI data set which will be used throughout the section to illustrate our methods.

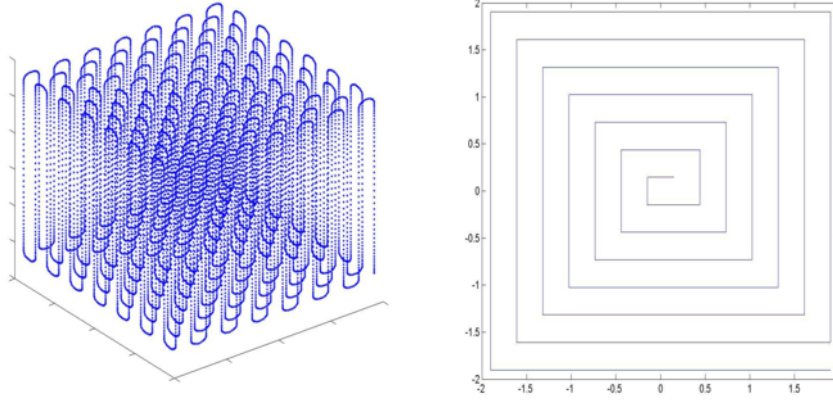


Figure 2. Left: 3D EVI Trajectory in a Cube in the Center of  $k$ -Space; Right: Projection of the Trajectory onto the Plane  $z = 0$  (a Square Spiral).

### 3.1 Activation paradigm and data set

The data were taken in the summer of 2006 at the Stanford MRI Lab in a fMRI experiment designed to track the hemodynamic signals in the brain while a subject underwent a visual-motor activation paradigm. The activation paradigm consisted of 15 cycles of 20 s length in time per cycle. At the beginning of each cycle, a 100 ms light flash was presented in front of the subject. The subject was instructed to press a button with the right thumb immediately after sensing the flash.

The EVI trajectory in Figure 2 was used to acquire data in each  $T_{shot} = 100$  ms time interval throughout the experiment. Within the  $k$ -space trajectory, we use the data in a  $14 \times 14 \times 46$  array representing measurements of (2.1) in  $14 \times 14$  line segments of length  $17\Delta_k$  in the  $z$ -direction in  $k$ -space. Since the EVI trajectory has to slow down at the end of each line segment to make a half circle turn, the positions of the 46 points in the  $k$ -space line segment are symmetric about  $z = 0$  but not equally spaced in the  $z$ -direction. For each visual-motor activation cycle, 200 such arrays were obtained. The data in the first cycle out of the 15 were thrown out. Thus, the raw data contain  $14 \times 200 = 2800$  complex arrays of dimension  $14 \times 14 \times 46$ . In addition,  $T_2$ -weighted FSE scans were obtained for anatomic reference.

### 3.2 Image reconstruction

After data collection, the raw  $k$ -space data was reconstructed into images of size  $64 \times 64 \times 64$  for each of the  $14 \times 200 = 2800$  time points in the unit of 100 ms. Since this is done for the individual readout periods, the image reconstruction algorithm is a map from  $14 \times 14 \times 46$  arrays to  $64 \times 64 \times 64$  images.

In keyhole MRI [27, 6], which also samples a central portion of  $k$ -space, the data are first regridded to  $\{S_d(\mathbf{k}), \mathbf{k} \in A_d\}$  for a certain hyperrectangular subset  $A_d$  of the cubic lattice  $\Omega_d^*$  in (2.4) with span  $\Delta_k$  and then the FFT is directly

used to reconstruct the image as

$$(3.1) \quad f(\mathbf{v}) \approx \sum_{\mathbf{k} \in A_d} S_d(\mathbf{k}) \exp(-i\mathbf{v}'\mathbf{k}) / \text{FOV}^3$$

for all voxels  $\mathbf{v}$  in the  $64 \times 64 \times 64$  lattice  $\Omega_d$  in the image space with span  $\text{FOV}/64$ . In addition to the noise in the raw data and approximation errors with (2.1) and (2.3), the sources of error in (3.1) include regridding and the contributions of the unobserved  $S_d(\mathbf{k})$  with  $\mathbf{k} \in \Omega_d^* \setminus A_d$ , in view of (2.4).

We use the prolate-spheroidal wave function (PSWF) to recover the images from  $k$ -space data [24, 30, 11]. Let  $A^\circ$  be the  $14 \times 14 \times 46$  set in  $k$ -space in which the data are taken. Let  $w(\mathbf{k})$  be the function on  $A^\circ$  which maximizes

$$(3.2) \quad \lambda_B = \max \int_B \left| \sum_{\mathbf{k} \in A^\circ} w(\mathbf{k}) \exp(-i\mathbf{v}'\mathbf{k}) \right|^2 d\mathbf{v}$$

subject to the normalization  $\int_\Omega \left| \sum_{\mathbf{k} \in A^\circ} w(\mathbf{k}) \exp(-i\mathbf{v}'\mathbf{k}) \right|^2 d\mathbf{v} = 1$ , where  $\Omega$  is a cubic domain of the spin density and  $B$  is a convex region in  $\Omega$  for which a high  $\lambda_B$  is attained. The PSWF is defined as

$$(3.3) \quad \phi(\mathbf{v}) = \sum_{\mathbf{k} \in A^\circ} w(\mathbf{k}) \exp(-i\mathbf{v}'\mathbf{k}) / C_w,$$

where  $C_w = \int_\Omega \sum_{\mathbf{k} \in A^\circ} w(\mathbf{k}) \exp(-i\mathbf{v}'\mathbf{k}) d\mathbf{v}$ . It follows that the PSWF is standardized to  $\int_\Omega \phi(\mathbf{v}) d\mathbf{v} = 1$  and concentrates in  $B$  with  $\lambda_B = \int_B |\phi(\mathbf{v})|^2 d\mathbf{v} / \int_\Omega |\phi(\mathbf{v})|^2 d\mathbf{v} \approx 1$ . When the region  $B$  is a product of an  $xy$ -set and a  $z$ -set, the PSWF can be decomposed as a product of two PSWFs in  $(x, y)$  and in  $z$ , since  $A^\circ$  is a product of intervals in the  $x$ -,  $y$ - and  $z$ -directions. Figure 3 plots the  $xy$ - and  $z$ -factors of such a 3D-PSWF with concentration  $\lambda_B = 0.95$ .

We estimate the spin density as

$$(3.4) \quad \hat{f}(\mathbf{v}) = \sum_{\mathbf{k} \in A^\circ} w(\mathbf{k}) S(\mathbf{k}) \exp(-i\mathbf{v}'\mathbf{k}) / C_w, \quad \mathbf{v} \in \Omega.$$

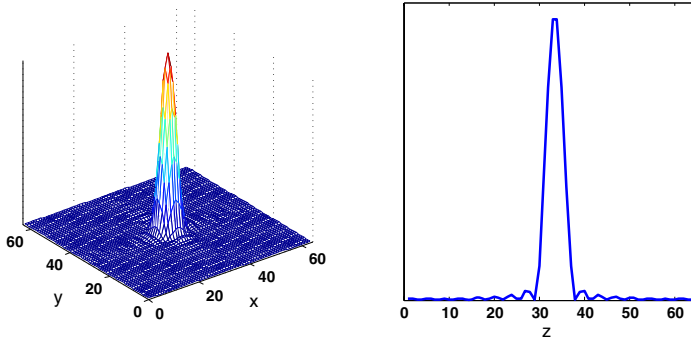


Figure 3. Two Factors of a 3 Dimensional Prolate-Spheroidal Kernel with Eigenvalue  $\lambda_B = 0.95$  for a  $14 \times 14 \times 46$  Sampling Region  $A^\circ$  in  $k$ -Space. Left: the  $xy$ -Factor; Right: the  $z$ -Factor. Although  $A^\circ$  Covers Only a Small Fraction of  $k$ -Space, the Kernel Is Still Reasonably Concentrated, Providing Adequate Spatial Resolution in Our Experiments.

It follows from (2.1) and (3.3) that the above estimator is approximately the convolution of the spin density and the PSWF:

$$(3.5) \quad \begin{aligned} \hat{f}(\mathbf{v}) &\approx \sum_{\mathbf{k} \in A^\circ} w(\mathbf{k}) f^*(\mathbf{k}) \exp(-i\mathbf{v}'\mathbf{k}) / C_w \\ &= \int_{\Omega} f(\mathbf{u}) \phi(\mathbf{v} - \mathbf{u}) d\mathbf{u}. \end{aligned}$$

Since the PSWF concentrates in  $B$  with  $\lambda_B \approx 1$ , the size of  $B$  is viewed as the spatial resolution of the reconstructed image (3.4). Compared with the slower full scan in the entire  $k$ -space, the loss of spatial resolution in (3.5) is similar to smoothing the image post data acquisition, which is typically done anyway in fMRI data analysis. The main difference between (3.4) and (3.1) is the optimality of the kernel  $\phi(\cdot)$  in (3.5) under the criterion (3.2).

### 3.3 Statistical analysis and visualization

After image reconstruction with (3.4), each  $14 \times 14 \times 46$  array of the  $k$ -space data is mapped to a  $64 \times 64 \times 64$  image, resulting in a time series of length  $14 \times 200 = 2800$  for each of the  $64^3$  voxels. We analyze these time courses individually in two steps, respectively for the BOLD positive rise signal and then the negative dip [13, 14].

#### 3.3.1. Analysis of the positive rise signal

We model the time course for the  $i$ -th voxel, for fixed  $i = 1, \dots, 64^3$ , as the sum of a hemodynamic component, the derivative of the hemodynamic component, a quadratic

drift component, and a seasonal component:

$$(3.6) \quad \begin{aligned} Y_i(t) &= \alpha_{i1} \sum_{u=1}^t h(t-u) \chi(u) + \alpha_{i2} \sum_{u=1}^t \dot{h}(t-u) \chi(u) \\ &\quad + \sum_{j=0}^2 \beta_{ij} t^j + \sum_{j=1}^d \gamma_{ij} I\{t = j(\text{mod } d)\} + \epsilon_i(t), \end{aligned}$$

where  $t = 1, \dots, 2800$  is the time in the unit of 100 ms,  $h(\cdot)$  is a standard hemodynamic response function (HRF),  $\dot{h}(\cdot)$  is the derivative of the HRF, and  $d$  is the period of seasonal effects present in the fMRI time course. Here  $\chi(u)$  is the known stimulus function which takes the value 1 if a stimulus is present and 0 otherwise. The derivative of the HRF is included to capture small temporal shifts in the onset of activation in individual voxels [5, 9]. The errors  $\epsilon_i(t)$  are assumed to form a stationary sequence in  $t$ , e.g. an AR or ARMA process.

In our analysis of the 2006 Stanford data [13, 14], the SPM double gamma HRF is used,  $d = 30$  is empirically chosen (globally for all  $i$ ) to capture the dominant seasonal effects due to respiration, and  $\epsilon_i(t)$  is treated as an AR(2) process. Estimates of the parameters  $\alpha_{ij}$ ,  $\beta_{ij}$ ,  $\gamma_{ij}$  and the unknown parameters of the AR(2) error process are obtained using the general linear model (GLM) approach [28]. Thus, for each voxel the time series is decomposed into drift, seasonal and hemodynamic components as illustrated in Figure 4.

We treat the parameter  $\alpha_{i1}$  in the time-course model (3.6) as the size of the positive-rise BOLD signal. We compute the  $t$ -statistics for  $\alpha_{i1}$  under the GLM in individual voxels and adjust their significance for multiple comparisons using the 10% false discovery rate [1, 7]. The time-to-rise of the significant voxels is estimated and plotted over the anatomic reference images as demonstrated in the top row of Figure 5. A clear activation pattern is present both in the visual and motor cortices in the figure as would be expected. Moreover, the time-to-rise is consistent with the experimental paradigm, since it appears in the visual cortex prior to the motor cortex.

#### 3.3.2. Analysis of the negative dip signal

For voxels that were deemed active in the GLM analysis for the positive rise, their respective time courses were analyzed further for the negative dip signal. This is done based on the hemodynamic component of each time course as illustrated in row D of Figure 4, after removing the drift and seasonal components.

For each active voxel, estimates of the amplitude and timing of the maximum dip (between the onset of the stimulus to the onset of the rise) were obtained. A bootstrap test for the amplitude of the negative dip was performed by resampling the 14 stimulus cycles, and the estimated time-to-dip for voxels with significant dip ( $p$ -value  $< 0.05$ ) is plotted over the anatomic reference images as demonstrated in the

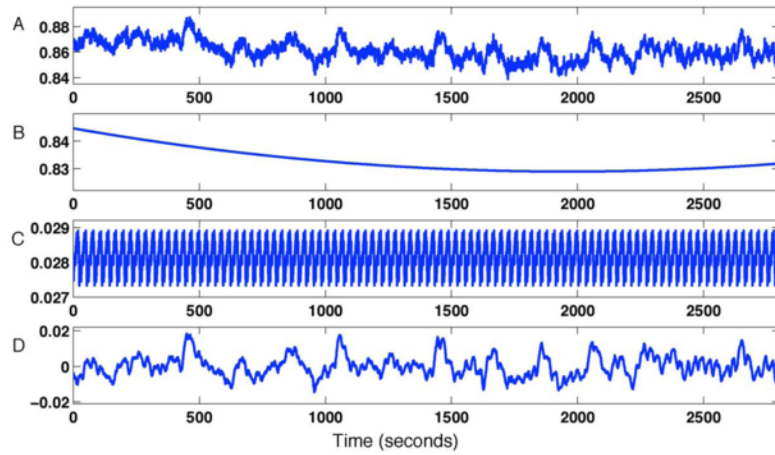


Figure 4. (A) A Typical Time Course Decomposed into (B) Quadratic Drift, (C) Periodic Nuisance Parameters and (D) fMRI Signal. The Length of the Period for the Nuisance Parameters Is Approximately 3 Seconds and Represents Artifacts Due to Respiration.

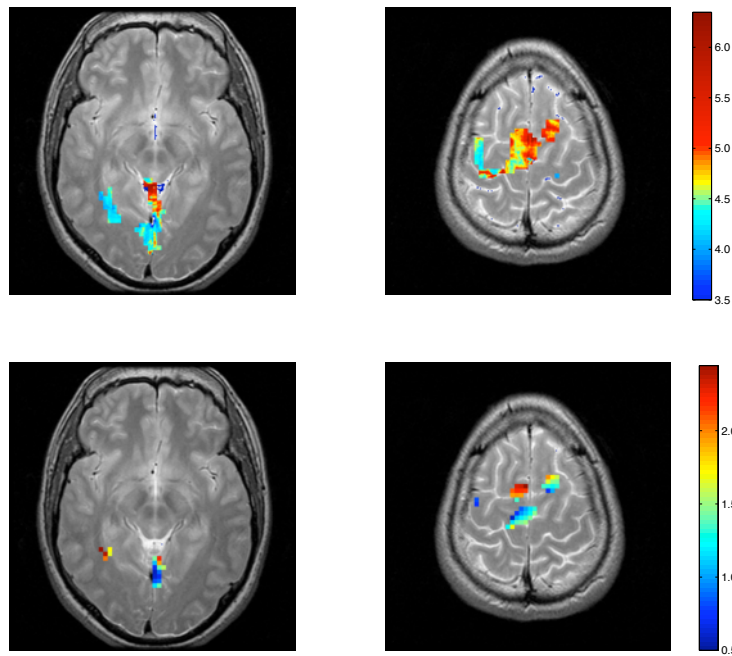


Figure 5. (Top Row) Maps of the Time-to-Rise in Voxels with Significant Activation for Two Slices in the Visual-Motor Experiment. A Slice Containing the Visual Cortex Is Shown to the Left and One Showing the Motor Cortex to the Right. The Results Indicate that the Rise Appears Earlier in the Visual then the Motor Cortex. (Bottom Row) Maps of the Time-to-Dip in Voxels with Significant Dips for the Same Two Slices. The Dip Appears Earlier in the Visual then the Motor Cortex.

bottom row of Figure 5. Again, a clear activation pattern is present both in the visual and motor cortices and the time-to-dip is consistent with the experiment paradigm.

Figure 6A shows the averages for two time courses extracted from the centers of the visual and motor cortices, respectively. We clearly see that the HRF estimated from

the visual cortex proceeds the one estimated from the motor cortex in time. Figure 6B shows a close-up of the first 3 seconds following activation. A negative dip appears first in the visual cortex. This makes sense since the visual cortex is logically the first region of the brain that begins to work on the image. After a few hundred milliseconds we see a de-

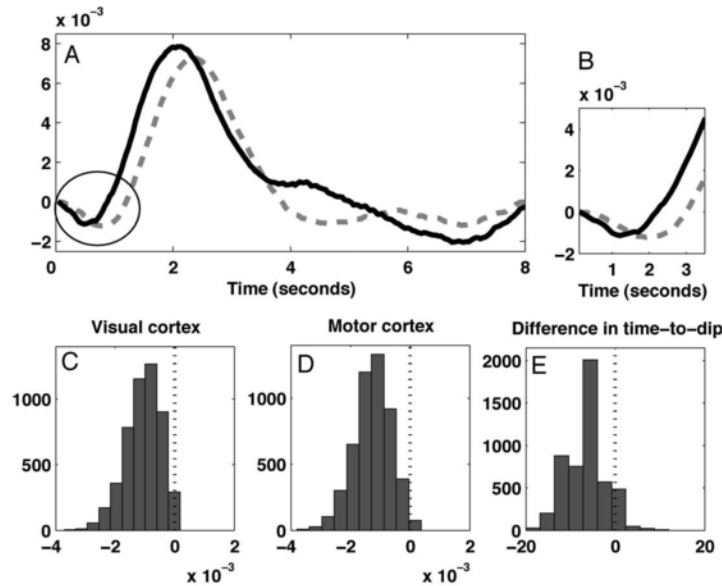


Figure 6. (A) Time Courses from the Visual (Bold) and Motor (Dashed) Cortices Averaged Over the 14 Cycles of the Visual-Motor Stimulus. (B) The First 3 Seconds Following Stimulation for the Two Time Courses Appearing in (A). The Dip Appears Earlier in the Visual Cortex than the Motor Cortex, which Is Consistent with the Experimental Paradigm. (C, D, E) The Results of Bootstrap Tests Show Significant Dips in Both the Visual and Motor Cortices, as Well as a Significant Difference in Time-to-Dip Between the Two Regions.

layed negative response in the motor cortex. Bootstrap tests (Figure 6C, D, E) confirm these results, and show that while both dips are significant, the dip in the visual cortex occurs at a significantly earlier time point compared to that of the motor cortex. In this experiment both the timing of the dip and rise give compelling evidence that neuronal activity is taking place in the visual cortex prior to the motor cortex as would be expected by the experimental paradigm.

## 4. DISCUSSION

Functional MRI is expected to greatly advance our understanding of brain function. However, in order to fully realize the potential of this technology, especially in higher human cognition, the time resolution of the present standard technique has to be improved. This paper describes the methodologies we have developed toward this goal and presents some of our results. We are excited with the progress we have made so far, but fMRI remains an extremely challenging area of research. In what follows, we discuss fMRI at 7 T, time sequence of brain activations, and multiple receiver coils.

### 4.1 Time sequence of brain activations

Compared with detecting brain activations, it is certainly a more difficult problem to ascertain the time sequence of activities in different parts of the brain. We have discussed the importance of this more difficult problem in the introduction and have argued that the positive rise BOLD signal

is too slow for this endeavor. Here we present some supporting evidence.

We conducted a second experiment in the summer of 2006 at the Stanford MRI Lab with the following auditory-motor-visual stimulation paradigm. At the beginning of each cycle, a tone was sounded through headphones which a subject was wearing. The subject was instructed to press a button with the right thumb immediately after hearing the tone. Upon pressing the button a 100 ms light flash was presented in front of the subject.

A purpose of this second experiment is to study the ability of the MRI signals to detect the reverse order of the activations at the motor and visual cortices, compared with the first experiment described in Section 3.1. The exact same statistical analysis was repeated for the auditory-motor-visual paradigm. It is important to note that in this second experiment, the order of activation should now be auditory, followed by motor, followed by visual. While the signal in the auditory does appear to peak first, there appears to be confounding in the timing of the peaks in the visual and motor cortices. This can be seen in Figure 7A where clearly the signal over the motor cortex peaks *after* the visual cortex. However, studying the dip alleviates this confounding, which can be seen more clearly in Figure 7B. The difference in the time-to-dip between the visual and motor cortices is not statistically different from zero. This is hardly surprising as the visual stimulus appears immediately after the button press. Included in Figure 7 is also the signal over the audi-

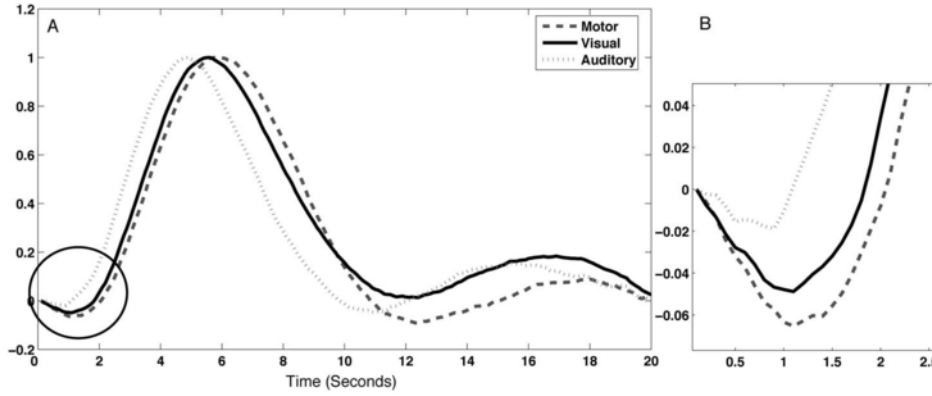


Figure 7. (A) Time Courses from the Auditory (Dotted), Visual (Bold) and Motor (Dashed) Cortices Averaged Over the 14 Cycles. (B) The First 3 Seconds Following Stimulation for the Three Time Courses Appearing in (A). The Dip Appears First in the Auditory Cortex, Followed by the Visual and Motor Cortices which Are Not Statistically Differentiable. The Rise in the Motor Signal Appears After the Rise in the Visual Signal which Implies an Incorrect Temporal Ordering of Activation.

tory cortex, whose dip and rise both peak prior to that of the visual and motor cortices as expected.

## 4.2 Multiple receiver coils

Multi-coil systems have been used to improve the spatial and temporal resolutions of MRI [25, 23, 22]. For a single readout period, multi-coil MRI data can be viewed as

$$(4.1) \quad \int_{\Omega} g_j(\mathbf{v})f(\mathbf{v}) \exp(i\mathbf{v}'\mathbf{k})d\mathbf{v} + \text{error}, \quad \mathbf{k} \in A^o, \quad j = 1, \dots, m,$$

where  $\Omega$  is the domain of the image,  $A^o$  is the sampled subset of  $k$ -space,  $g_j(\mathbf{v})$  is the spatial sensitivity of the  $j$ -th coil, and  $m$  is the total number of receiver coils. The spatial sensitivities  $g_j(\mathbf{v})$  are fixed and assumed to be known, since they can be accurately estimated from anatomical data.

In sensitivity encoding (SENSE), receiver coils with different spatial sensitivities  $g_j(\mathbf{v})$  are used to reduce the sampled  $k$ -space points and thus to improve the time resolution. This is achieved by increasing the span of the sampled  $k$ -space lattice while maintaining their maximum extent, as shown in the following idealized example. For standard 2D MRI with a single coil ( $m = 1$  and smooth  $g_1(x) \approx 1$ ), the trajectory  $\mathbf{k}(t)$  traverses through the entire 2D lattice  $\Delta_k\{-63, \dots, 64\}^2$  in  $k$ -space and the Fourier inversion of (4.1) is used to reconstruct  $g_1(x)f(x)$ , where  $\Delta_k = 2\pi/\text{FOV}$  is the distance between the sampled  $k$ -space points and FOV is the diameter of  $\Omega$ . By doubling  $\Delta_k$  to  $\Delta'_k = 4\pi/\text{FOV}$ , SENSE uses a trajectory  $\mathbf{k}(t)$  traversing through the lattice  $\Delta'_k\{-31, \dots, 32\}^2$  to attain a nominal  $128 \times 128$  spatial resolution. A heuristic argument for this boosting of the spatial resolution is as follows. If the diameter of the support of each  $g_j$  is about one half of the diameter of the 2D image space  $\Omega$ , then the field of view for each coil is halved, resulting in a  $\Delta_k$  twice as large. Another heuristic argument is to use all  $g_j(x)e^{i\mathbf{x}'\mathbf{k}}$  with different  $j$  and  $\mathbf{k}$

as a richer basis in image reconstruction when the domains of  $g_j$  overlap. The validity of these arguments remains to be carefully studied in fMRI, since the choice of the spatial sensitivities  $g_j(\mathbf{v})$  is limited by the location, shape and other physical constraints of receiver coils. Nevertheless, multi-coil system is an important direction for further development and improvement of the current fMRI technology.

## 4.3 Fast fMRI at 7 T

There is some controversy about the question of whether 7 T imaging will be more or perhaps less useful for fMRI. Physicists who believe it will be less useful have pointed out that fMRI at 7 T would suffer diminished response and lower SNR due to the increased susceptibility artifact and the fact that the wavelength corresponding to the resonant frequency at 7 T is comparable with the skull diameter. However, more optimistic physicists still believe in the possibility of overcoming these difficulties with better coils and better images at 7 T. Thus, the next phase of our work is to conduct 7 T fMRI experiments at multiple labs to resolve this feasibility question.

Received 5 March 2008

## REFERENCES

- [1] Benjamini, Y. and Hochberg, Y. (1995). Controlling the false discovery rate: A practical and powerful approach to multiple testing. *Journal of the Royal Statistical Society, Series B* **57** 289–300. [MR1325392](#)
- [2] Cho, Z. H., Ro, Y. M. and Lim, T. H. (1992). NMR venography using the susceptibility effect produced by deoxyhemoglobin. *Magnetic Resonance in Medicine* **28** 25–38.
- [3] Duong, T. Q., Kim, D. S., Ugurbil, K. and Kim, S. G. (2000). Spatio-temporal dynamics of the BOLD fMRI signals: Toward mapping columnar structures using the early negative response. *Magnetic Resonance in Medicine* **44** 231–242.
- [4] Ernst, T. and Hennig, J. (1994). Observation of a fast response in functional MR. *Magnetic Resonance in Medicine* **32** 146–149.

- [5] Friston, K. J., Josephs, O., Rees, G. and Turner, R. (1998). Non-linear event-related responses in fMRI. *Magnetic Resonance in Medicine* **39**(1) 41–52.
- [6] Gao, J. H., Xiong, J., Lai, S., Haacke, E. M., Woldorff, M. G., Li, J. and Fox, P. T. (1996). Improving the temporal resolution of functional MR imaging using keyhole techniques. *Magnetic Resonance in Medicine* **35** 854–860.
- [7] Genovese, C. R., Lazar, N. A. and Nichols, T. E. (2002). Thresholding of statistical maps in functional neuroimaging using the false discovery rate. *NeuroImage* **15** 870–878.
- [8] Harvey, P. R. and Mansfield, P. (1996). Echo-volumar imaging (EVI) at 0.5 T: First whole-body volunteer studies. *Magnetic Resonance in Medicine* **35** 80–88.
- [9] Henson, R. N., Price, C. J., Rugg, M. D., Turner, R. and Friston, K. J. (2002). Detecting latency differences in event-related BOLD responses: Application to words versus nonwords and initial versus repeated face presentations. *NeuroImage* **15**(1) 83–97.
- [10] Kim, D. S., Duong, T. Q. and Kim, S. G. (2000). High-resolution mapping of iso-orientation columns by fMRI. *Nature Neuroscience* **3**(2) 164–169.
- [11] Lindquist, M. A. (2003). Optimal data acquisition in fMRI using prolate spheroidal wave functions. *International Journal of Imaging Systems and Technology* **13** 803–812.
- [12] Lindquist, M. A., Zhang, C.-H., Glover, G., Shepp, L. and Yang, Q. X. (2006). A generalization of the two dimensional prolate spheroidal wave function method for non-rectilinear MRI data acquisition methods. *IEEE Trans. Image Processing* **15**(9) 2792–2804.
- [13] Lindquist, M., Zhang, C.-H., Glover, G. and Shepp, L. (2008). Rapid three-dimensional functional magnetic resonance imaging of the initial negative BOLD response. *J. Magnetic Resonance* **191** 100–111.
- [14] Lindquist, M., Zhang, C.-H., Glover, G. and Shepp, L. (2007). Acquisition and statistical analysis of rapid 3D fMRI data. *Statistica Sinica*, in press.
- [15] Malonek, D. and Grinvald, A. (1996). The imaging spectroscopy reveals the interaction between electrical activity and cortical microcirculation: Implication for optical, PET and MR functional brain imaging. *Science* **272** 551–554.
- [16] Mansfield, P., Coxon, R. and Hykin, J. (1995). Echo-volumar imaging (EVI) at 3.0 T: First normal volunteer and functional imaging results. *Journal of Computer Assisted Tomography* **19**(6) 847–852.
- [17] Mansfield, P., Howseman, A. M. and Ordidge, R. J. (1989). Volumar imaging using NMR spin echos: Echo-volumar imaging (EVI) at 0.1 T. *Journal of Physics E* **22** 324–330.
- [18] Menon, R. S., Ogawa, S., Hu, X., Strupp, J. S., Andersen, P. and Ugurbil, K. (1995). Bold based functional MRI at 4 Tesla includes a capillary bed contribution: Echo-planar imaging mirrors previous optical imaging using intrinsic signals. *Magnetic Resonance in Medicine* **33** 453–459.
- [19] Ogawa, S., Lee, T. M. and Barrere, B. (1993). The sensitivity of magnetic resonance image signals of a rat brain to changes in the cerebralvenous blood oxygenation. *Magn. Reson. Med.* **29** 205–210.
- [20] Ogawa, S., Menon, R. S., Tank, D. W., Kim, S. G., Merkle, H., Ellerman, M. and Ugurbil, K. (1993). Functional brain mapping 1 blood oxygenation level-dependent contrast magnetic resonance imaging: A comparison of signal characteristics with biophysical models. *Biophys. J.* **64** 803–812.
- [21] Ogawa, S., Tank, D. W., Menon, R., Ellermann, J. M., Kim, S. G., Merkle, H. and Ugurbil, K. (1992). Intrinsic signal changes accompanying sensory stimulation: Functional brain mapping with magnetic resonance imaging. *Proc. Natl. Acad. Sci. USA* **89** 5951–5955.
- [22] Pruessmann, K. P. (2006). Encoding and reconstruction in parallel MRI. *NMR in Biomedicine* **19** 288–299.
- [23] Pruessmann, K. P., Weiger, M., Scheidegger, M. B. and Boesiger, P. (1999). SENSE: Sensitivity encoding for fast MRI. *Magnetic Resonance in Medicine* **42**(5) 952–956.
- [24] Shepp, L. and Zhang, C.-H. (2000). Fast functional magnetic resonance imaging via prolate wavelets. *Appl. Comput. Harmonic Analysis* **9** 99–119. [MR1777121](#)
- [25] Sodickson, D. K. and Manning, W. J. (1997). Simultaneous acquisition of spatial harmonics (SMASH): Fast imaging with radiofrequency coil arrays. *Magnetic Resonance in Medicine* **38**(4) 591–603.
- [26] Thompson, J. K., Peterson, M. R. and Freeman, R. D. (2004). High-resolution neurometabolic coupling revealed by focal activation of visual neurons. *Nature Neuroscience* **7** 919–920.
- [27] van Vaals, J. J., Brummer, M. E., Dixon, W. T., Tuithof, H. H., Engels, H., Nelson, R. C., Gerety, B. M., Chezmar, J. L. and den Boer, J. A. (1993). Keyhole method for accelerating imaging of contrast agent uptake. *J. Magn. Reson. Imaging* **3** 671–675.
- [28] Worsley, K. J. and Friston, K. J. (1995). Analysis of fMRI time-series revisited-again. *NeuroImage* **2** 173–181.
- [29] Yacoub, E., Le, T. H. and Hu, X. (1998). Detecting the early response at 1.5 Tesla. *NeuroImage* **7** S266.
- [30] Yang, Q. X., Lindquist, M. A., Shepp, L., Zhang, C.-H., Wang, J. and Smith, M. B. (2002). Two dimensional prolate spheroidal wave functions for MRI. *J. Magnetic Resonance* **158** 43–51.

Cun-Hui Zhang  
 Department of Statistics and Biostatistics  
 Hill Center, Busch Campus  
 Rutgers University  
 Piscataway, NJ 08854, USA  
 E-mail address: [czhang@stat.rutgers.edu](mailto:czhang@stat.rutgers.edu)

Martin A. Lindquist  
 Department of Statistics  
 Columbia University  
 New York, NY 10027, USA  
 E-mail address: [martin@stat.columbia.edu](mailto:martin@stat.columbia.edu)

Zang-Hee Cho  
 Neuroscience Research Institute  
 Gachon University of Medicine and Science  
 Incheon, Korea  
 E-mail address: [zcho@gachon.ac.kr](mailto:zcho@gachon.ac.kr)

Gary Glover  
 Department of Radiology  
 Stanford University  
 Stanford, CA 94305, USA  
 E-mail address: [gary@lucas.stanford.edu](mailto:gary@lucas.stanford.edu)

Lawrence Shepp  
 Department of Statistics and Biostatistics  
 Hill Center, Busch Campus  
 Rutgers University  
 Piscataway, NJ 08854, USA  
 E-mail address: [shepp@stat.rutgers.edu](mailto:shepp@stat.rutgers.edu)